A coupled Volume of Fluid and Immersed Boundary Method for simulating 3D multiphase flows with contact line dynamics in complex geometries

Patel, H.V.; Das, S.; Kuipers, J.A.M.; Padding, J. T.; Peters, E.A.J.F.

DOI
10.1016/j.ces.2017.03.012

Publication date
2017

Document Version
Final published version

Published in
Chemical Engineering Science

Chemical Engineering Science 166 (2017) 28–41

Contents lists available at ScienceDirect

Chemical Engineering Science

journal homepage: www.elsevier.com/locate/ces

A coupled Volume of Fluid and Immersed Boundary Method for simulating 3D multiphase flows with contact line dynamics in complex geometries

H.V. Patel [a], S. Das [a], J.A.M. Kuipers [a], J.T. Padding [a,b], E.A.J.F. Peters [a,*]

[a] Multiphase Reactors Group, Department of Chemical Engineering and Chemistry, Eindhoven University of Technology, P.O. Box 513, 5600 MB Eindhoven, The Netherlands
[b] Intensified Reaction and Separation Systems, Department of Process and Energy, Delft University of Technology, Leeghwaterstraat 39, 2628 CB Delft, The Netherlands

HIGHLIGHTS

- We present a 3D coupled VOF and sharp interface-implicit IBM for multiphase flows.
- Contact line dynamic is resolved by applying a contact angle boundary conditions.
- Extensive validation cases are presented for static and dynamic contact angles.
- The simulated contact line dynamics with and without using IBM are compared.
- Pore-scale water flooding process through BCC and FCC structures are presented.

ARTICLE INFO

Article history:
Received 14 December 2016
Received in revised form 1 March 2017
Accepted 3 March 2017
Available online 6 March 2017

Keywords:
Volume of Fluid (VOF)
Immersed Boundary Method (IBM)
Static and dynamic contact angle
Contact line dynamics
Water flooding
Enhanced Oil Recovery (EOR)

ABSTRACT

A numerical methodology is presented for simulating 3D multiphase flows through complex geometries on a non-body conformal Cartesian computational grid. A direct forcing implicit immersed boundary method (IBM) is used to sharply resolve complex geometries, employing the finite volume method (FVM) on a staggered grid. The fluid-fluid interface is tracked by a mass conservative sharp interface volume of fluid (VOF) method. Contact line dynamics at macroscopic length scale is simulated by imposing the apparent contact angle (static or dynamic) as a boundary condition at the three-phase contact line. The developed numerical methodology is validated for several test cases including the equilibrium shape of a droplet on flat and spherical surfaces, the temporal evolution of a droplet spreading on a flat surface. The obtained results show an excellent correspondence with those derived analytically or taken from literature. Furthermore, the present model is used to estimate, on a pore-scale, the residual oil remaining in idealized porous structures after water flooding, similar to the process used in enhanced oil recovery (EOR).

1. Introduction

Multiphase flows in complex geometries are encountered widely in nature and technology. Examples include enhanced oil recovery (EOR) (Alvarado and Manrique, 2010), trickle bed reactors (Herskowitz and Smith, 1983), microfluidics devices (Stone et al., 2004) and biological systems (Fauci and Gueron, 2001).

Focusing on oil recovery, during the primary recovery process, oil comes out of the porous rocks automatically due to its own natural pressure. Gradually, the natural pressure of the oil reduces and the automatic flow of the oil stops. There is still a large amount of oil which remains trapped in the porous rocks. To recover this residual oil EOR processes are used. There is a wide variety of EOR processes available e.g. gas injection, thermal processes, water flooding, chemical flooding etc. and the choice is generally based on economy. In water flooding (Sheng, 2014) high pressure and/or high temperature water is pushed through porous rocks to recover residual oil. Focus of the current work is to devise a methodology for pore-scale simulations of oil-water multiphase flows through complex rock structures during such a water flooding process. To serve this purpose, three different things need to be resolved: (i) oil-water multi-fluid interface tracking, (ii) interactions between fluids (oil and water) and complex solid geometries, and (iii) three-phase contact line dynamics.

* Corresponding author.
E-mail address: E.A.J.F.Peters@tue.nl (E.A.J.F. Peters).

http://dx.doi.org/10.1016/j.ces.2017.03.012
0009-2509/

Accurate simulations of sharp interface multi-fluid flows are particularly difficult for the following reasons: (i) the fluid-fluid interface needs to be tracked accurately without introducing excessive computational smearing and (ii) accurate calculation of surface tension force is necessary in case of highly curved interfaces. A wide range of numerical methods has been developed and successfully applied to a variety of multi-fluid flow problems (Wörner, 2003). The front tracking (FT) method (Tryggvason et al., 2001) uses triangular shaped markers (in 3D) on the Lagrangian interface to track it. However, the Navier-Stokes equations are solved on a fixed Eulerian grid. Necessary information is exchanged between the Lagrangian interface markers and neighboring Eulerian grid cells for advection of the interface and computation of the surface tension force. This method is very accurate, but it requires dynamic remeshing of the interface markers. Also, interface breakup and coalescence is not automatic and it requires a proper sub-grid model to resolve them. The level set (LS) method (Sussman et al., 1994) defines the interface as the zero level set of a distance function from the interface. A numerical solution is found for the advection of this distance function. The LS method is conceptually simple and relatively easy to implement but it suffers from loss of mass in case of highly deformed interfaces. The volume of fluid (VOF) method (Hirt and Nichols, 1981; Youngs, 1982) uses a color function $F(x,y,z,t)$ which denotes the fractional amount of particular fluid present at spatial location (x,y,z) at time t. Advection of F is governed by the same equation as for the LS method but it is solved by pseudo-Lagrangian geometrical advection schemes to minimize numerical diffusion. This particular feature makes VOF the most mass conservative among all multi-fluid interface tracking methods. Interface reconstruction is required for geometrical advection of F which is done by simple line interface calculation (SLIC) by Noh and Woodward (1976) or piecewise linear interface calculation (PLIC) by Youngs (1982). The accuracy of the PLIC algorithm is higher compared to SLIC and is used in the present work. A drawback of LS and VOF methods are that they produce numerical coalescence when two interfaces are less than one grid cell apart. The surface tension force (Baltussen et al., 2014) can be numerically calculated by the continuum surface force (CSF) model, height function model or tensile force model. The density-scaled CSF model proposed by Brackbill et al. (1992) is used here due to its simplicity and robustness especially in the presence of complex solid boundaries.

Fluid-fluid interfaces in contact with solid boundaries produce a three-phase contact line and thus the contact line dynamics needs to be resolved in addition to solving interface motion. The contact line behavior is determined by microscopic physicochemical interactions between molecules of two different immiscible fluids and the solid substrate, and it can drastically affect the statics and dynamics of the bulk flow (Snoeijer and Andreotti, 2013). The result of these microscopic interactions at the contact line can be seen as an apparent contact angle on macroscopic length scales. Multiple attempts have been made to describe the effect of the contact line on macroscopic length scales by giving a single/static (Renardy et al., 2001) or dynamic (Dussan, 1979) value for apparent contact angle. An interesting review on simulations with moving contact lines is presented by Sui et al. (2014) where the main approach is to apply the apparent contact angle as a boundary condition at the grid cells located at the contact line. However, the majority of the available literature focuses on the numerical simulations of the contact line dynamics for simple solid geometries on a body conformal grid and still a significant amount of work is needed for complex solid geometries.

The immersed boundary method (IBM) is a well-established computational technique which uses non-body conformal structured (mainly Cartesian) grids for simulating flow through complex geometries. The main advantages of IBM over the traditional unstructured body conformal grids are simplicity in grid generation and discretization of the Navier-Stokes equations, ease of code development, less memory requirement to store the grid information and higher computational efficiency. An excellent review is presented by Mittal and Iaccarino (2005) on the large variety of IBMs. The methods can be broadly classified in two categories: (i) continuous forcing approach, first proposed by Peskin (1972), where the no-slip condition at the immersed boundary (IB) is applied by introducing a continuous forcing function as a source term in the momentum equation and (ii) discrete (or direct) forcing approaches where the effect of the IB is imposed at the level of the discretized momentum equation. The direct forcing approach produces a sharp solid interface without spatial spreading. So, in the present work the direct forcing implicit IBM is used which is second order accurate, stable, easy to implement and does not require calibration of the geometry, which is useful for complex geometries.

Very few attempts have been made to integrate multi-fluid interface tracking methods with IBMs to simulate multiphase flows with contact line dynamics through complex solid geometries. Deen et al. (2009) used the FT method with direct forcing IBM to simulate interactions of bubbles with a solid particle bed. However, contact line dynamics was not incorporated in their simulations. Suh and Son (2009) used the LS method to describe both fluid-fluid and fluids-solid interface (IB) to simulate a piezoelectric inkjet process. The VOF method with IBM was used by Sun and Sakai (2016) to simulate flow through a twin screw kneader, Washino et al. (2011) for a wet granulation process and Karagadde et al. (2012) for modeling motion and growth of dendrites in a solidifying melt. However, the effect of the IB is explicitly imposed by modifying the velocity using local solid fractions which produces a diffuse fluids-solid interface.

In this paper, a methodology is presented to couple the VOF method with direct forcing, implicit and sharp interface IBM with contact line dynamics. The paper is organized as follows: First, we describe the governing Navier-Stokes and VOF advection equations for multiphase flows. Subsequently, numerical and implementation details are presented for the solution methodology, IBM, VOF and contact line dynamics. Next, an extensive validation of the current numerical model is reported for both static and dynamic contact angles. Last, we present our findings for numerical simulations of a water flooding process through periodic body centered cubic (BCC) and face centered cubic (FCC) structures and estimate the residual oil.

2. Governing equations

For incompressible multiphase flows the Navier-Stokes equations can be combined into a single equation for the velocity field $\mathbf{u}$ in the entire domain, taking into account the effect of surface tension by a local volumetric surface tension force $\mathbf{F}_\sigma$ accounting for the presence of a curved deformable fluid-fluid interface. The governing mass and momentum conservation equations for unsteady, incompressible, Newtonian, multiphase flows are expressed as follows:

$$\nabla \cdot \mathbf{u} = 0 \tag{1}$$

$$\rho \frac{\partial \mathbf{u}}{\partial t} + \rho \nabla \cdot (\mathbf{u}\mathbf{u}) = -\nabla p + \nabla \cdot \boldsymbol{\tau} + \rho \mathbf{g} + \mathbf{F}_\sigma \tag{2}$$

where $\boldsymbol{\tau} = \mu[\nabla \mathbf{u} + (\nabla \mathbf{u})^T]$ is the fluid stress tensor and $\mathbf{g}$ is the acceleration due to gravity. The local averaged density ρ and dynamic viscosity μ depend on the local fluid phase distribution and hence are evaluated from the local phase fraction F between

fluid phases. The volumetric surface tension force appearing in the momentum equation acts only in the vicinity of the interface. Advection of F is governed by the following equation:

$$\frac{DF}{Dt} = \frac{\partial F}{\partial t} + \mathbf{u} \cdot \nabla F = 0 \tag{3}$$

This equation expresses that the interface is advected with the local fluid velocity. To evaluate the local averaged density ρ, linear averaging of the densities of the fluid 1 ($F = 1$) and fluid 2 ($F = 0$) is used:

$$\rho = F\rho_1 + (1 - F)\rho_2 \tag{4}$$

Similarly, the local average dynamic viscosity μ could also be evaluated by linear averaging of the dynamic viscosities of individual fluid phase. Alternatively, following a fundamental approach proposed by Prosperetti (2002), the local average kinematic viscosity is evaluated by harmonic averaging of the kinematic viscosities of the individual fluid phases:

$$\frac{\rho}{\mu} = F\frac{\rho_1}{\mu_1} + (1 - F)\frac{\rho_2}{\mu_2} \tag{5}$$

In all the computations reported in this paper, Eqs. (4) and (5) are used to evaluate the local average density and dynamic viscosity, respectively.

3. Numerical details

In this section numerical details for the coupled VOF and IBM framework are presented. The section is divided into four main parts: (i) solution methodology focusing on discretization and numerical solution of the incompressible Navier-Stokes equations, (ii) IBM dealing with the dynamic interactions between fluids and non-deformable solids, (iii) VOF dealing with the dynamics of deformable fluid-fluid interface, and (iv) contact line dynamics dealing with the coupling of VOF and IBM by appropriate contact angle boundary condition.

3.1. Solution methodology

In the current implementation, the finite volume method (FVM) is used to solve the mass and momentum conservation equations in each control volume (CV) of a staggered computational grid. The time-discretized form of the momentum equation is obtained as:

$$\rho\mathbf{u}^{k+1} = \rho\mathbf{u}^{k} + \frac{\Delta t}{\Delta V}\left\{ -\int_A p^{k+1}\hat{\mathbf{s}}\,dA - \rho\int_A \left[\mathbf{C}^{k+1}_{\mathrm{FOU}} + \left(\mathbf{C}^{k}_{\text{min-mod}} - \mathbf{C}^{k}_{\mathrm{FOU}}\right)\right]dA + {}_A\boldsymbol{\tau}^{k,k+1}\cdot\hat{\mathbf{s}}\,dA \right\} + \Delta t\left\{\rho\mathbf{g}^{k} + \mathbf{F}^{k}_{\sigma}\right\} \tag{6}$$

where ΔV represents the volume of each CV, A and $\hat{\mathbf{s}}$ are surface area and outward pointing unit cell surface normal respectively, superscript k indicates the time index and $\mathbf{C}$ indicates the net-convective flux: $\mathbf{C} = (\mathbf{u}\cdot\hat{\mathbf{s}})\,\mathbf{u}$. A deferred correction method has been incorporated in the convection term, where both the first order upwind (FOU) scheme and total variation diminishing (TVD) min-mod scheme are used to calculate the convection flux; the flux by the FOU scheme ($\mathbf{C}_{\mathrm{FOU}}$) is treated implicitly and, based on the higher order min-mod scheme, a correction is introduced ($\mathbf{C}_{\text{min-mod}} - \mathbf{C}_{\mathrm{FOU}}$) which is treated in an explicit manner. A second order accurate central difference scheme is used for discretizing diffusive terms. The volumetric surface tension force is treated explicitly and its discretization is explained in the subsequent section. Eq. (6) is solved by a fractional step method, where at the first-step the tentative velocity field $\mathbf{u}^*$ is computed from:

$$\rho\mathbf{u}^{*} = \rho\mathbf{u}^{k} + \frac{\Delta t}{\Delta V}\left\{ -\int_A p^{k}\hat{\mathbf{s}}\,dA - \rho\int_A \left[\mathbf{C}^{*}_{\mathrm{FOU}} + \left(\mathbf{C}^{k}_{\text{min-mod}} - \mathbf{C}^{k}_{\mathrm{FOU}}\right)\right]dA + \int_A \boldsymbol{\tau}^{k,*}\cdot\hat{\mathbf{s}}\,dA \right\} + \Delta t\left\{\rho\mathbf{g}^{k} + \mathbf{F}^{k}_{\sigma}\right\} \tag{7}$$

Here the stress tensor is split into an implicit part and an explicit part. In the momentum equation for each of the 3 directions (i.e., x, y or z), only the velocity component in the direction under consideration is treated implicitly, whereas the other velocity components are treated explicitly. For Eq. (7) we need to solve a set of linear equations. The enforcement of the no-slip boundary condition at the IB wall is handled at the level of discretization of the momentum equation which is detailed in the next section. We use a robust and efficient Block-Incomplete Cholesky Conjugate Gradient (B-ICCG) solver that is OpenMP-parallelized to solve the resulting sparse matrix for each velocity component.

The velocity at the new time level $k+1$ can be obtained from:

$$\mathbf{u}^{k+1} = \mathbf{u}^{*} - \frac{\Delta t}{\rho}\nabla(\delta p) \tag{8}$$

where $\delta p = p^{k+1} - p^{k}$ represents the pressure correction. Since $\mathbf{u}^{k+1}$ needs to satisfy the continuity equation, the pressure Poisson equation is obtained as:

$$\nabla\cdot\left\{\frac{\Delta t}{\rho}\nabla(\delta p)\right\} = \nabla\cdot\mathbf{u}^{*} \tag{9}$$

which is again solved by the B-ICCG sparse matrix solver. The periodic boundary conditions for both velocity and pressure are taken care of during the flux calculation and treated implicitly in the sparse matrix solving steps. A detailed implementation of periodic boundary condition for pressure-velocity coupling is presented in Das et al. (2017). Note that the periodic boundary condition for the VOF method is applied in an explicit manner.

3.2. Immersed boundary method (IBM)

An implicit (direct) second-order accurate IBM proposed by Deen et al. (2012) and described in details by Das et al. (2017) has been used to apply no-slip boundary conditions for fluids-solid interactions at immersed boundaries. Initially, all the cells are marked/flagged as either 'solid-cell' (cell-center inside the solid body) or 'fluid-cell' (cell-center in the fluid zone) in the staggered computational grid. 'IB-cells' are a special type of fluid-cells, as they have at least one neighboring solid-cell. It is in these IB-cells where the no-slip boundary condition is imposed as shown in Fig. 1. Note that because staggered positions are used for the velocity components, the CV is different for different components. Fig. 1 shows an example for the case of the x-component of the velocity. The algebraic form of the discretized momentum equation, Eq. (7), at the CV center c can be represented as:

$$a_c\phi_c + \sum_{nb} a_{nb}\phi_{nb} = b_c \tag{10}$$

where ϕ corresponds to one of the fluid velocity components and nb indicates the cell-center of surrounding neighboring cells. a represents the fluids- and geometry-dependent matrix coefficients and all the explicit terms are collected in b_c. From the perspective a fluid-cell c, if one of the surrounding cells nb is a solid-cell, the no-slip condition is imposed by changing the central coefficient (a_c) and neighboring coefficient (a_{nb}) of Eq. (10).

An example is given in Fig. 1, where a fluid-cell c is neighboring a solid-cell w. The value of ϕ in the solid-cell is expressed as a linear combination of relevant fluid-cell values, in such a way that it satisfies the no-slip boundary condition at the solid surface (s). For this purpose a quadratic interpolation polynomial is used:

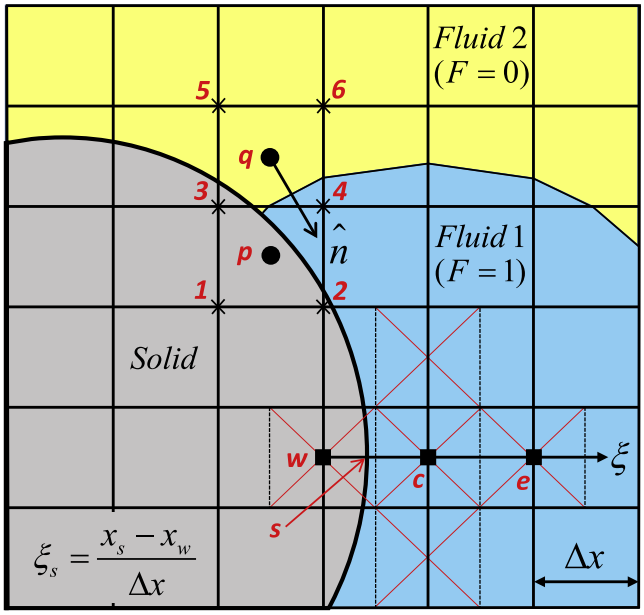

Fig. 1. 2D schematic representation of the fluid-fluid interface in contact with a solid surface in a Cartesian computational grid to illustrate implementation details. ● = scalar (pressure/phase fraction) CV, ■ = x-velocity CV on the staggered grid and × = cell vertices. Interface between two fluids is piecewise linear according to the PLIC algorithm.

$\phi = p\,\xi^2 + q\,\xi + r$, where ξ is a non-dimensional distance from solid-cell w, as shown in Fig. 1. The values of the coefficients p, q and r are obtained from the known values of ϕ at the solid boundary ($\phi = 0$ at $\xi = \xi_s$) and the two nodes in the fluid ($\phi = \phi_c$ at $\xi = 1$ and $\phi = \phi_e$ at $\xi = 2$). As a result we find the extrapolated value:

$$\phi_w = -\frac{2\xi_s}{1-\xi_s}\phi_c + \frac{\xi_s}{2-\xi_s}\phi_e \tag{11}$$

where ξ_s corresponds to the non-dimensional distance from the solid-cell to the point where the grid line intersects the solid boundary. The modified coefficients ($\hat{a}$) for Eq. (10) become

$$\begin{aligned}\hat{a}_c &= a_c + a_w\left(-\frac{2\xi_s}{1-\xi_s}\right)\\ \hat{a}_e &= a_e + a_w\left(-\frac{\xi_s}{2-\xi_s}\right)\\ \hat{a}_w &= 0\end{aligned} \tag{12}$$

Note that Eq. (10) is also solved for solid-cells. To enforce zero velocity for the solid-cells, central coefficient (a_c) is modified to 1 and all other coefficients (i.e. a_{nb}, b_c) to 0. For a complex geometry it is also possible that a fluid-cell near the immersed boundary has more than one neighbor lying inside a solid body. In that case the implementation details are more involved and readers are referred to Das et al. (2017).

3.3. Volume of Fluid (VOF)

The VOF part of the simulation consists of three main subparts: (i) solution of fluid phase fraction F-advection equation, (ii) computation of the volumetric surface tension force, and (iii) smoothing of fluid phase fraction F.

3.3.1. Solution of fluid phase fraction F-advection equation

The integration of the hyperbolic F-advection equation, Eq. (3), is the most critical part of the VOF model and is based on geometrical advection which can be viewed as a pseudo-Lagrangian advection step. The advantage of the geometrical advection is given by the fact that a sharp interface is maintained during the simulations. First, for each Eulerian cell containing an interface the unit normal vector $\hat{\mathbf{n}}$ to the interface is estimated from the gradient of the fluid phase fraction F as

$$\hat{\mathbf{n}} = \frac{\nabla F}{|\nabla F|} \tag{13}$$

In our model first the components of the normal vector are computed at the vertices of the Eulerian cell and then the cell-centered components are computed by averaging over the eight (four in 2D) surrounding vertices. An example is given for a 2D case in Fig. 1, where $\hat{\mathbf{n}}$ at cell-center q is computed by averaging $\hat{\mathbf{n}}$ over vertices 3, 4, 5 and 6. Note that the direction of $\hat{\mathbf{n}}$ points from fluid 2 ($F = 0$) towards fluid 1 ($F = 1$).

By combining the information of the normal direction in an Eulerian cell and its phase fraction F the PLIC surface cutting through the Eulerian cell is constructed. Here transformations of the coordinate system are applied to reduce the number of possible configurations of a PLIC surface from 64 to 5 generic configurations. These steps are described with all necessary geometrical and mathematical details by Van Sint Annaland et al. (2005).

Note that F-advection is carried out for all fluid-cells. In presence of immersed boundaries the VOF method is no longer conservative as a small local mass error may occur due to the presence of partially filled cells at boundaries, which may further accumulate over time. If strict mass conservation is needed, we find the mass error after each time step and compensate for it by subtracting the mean mass error from each cell at the interface (i.e. cells where $0 < F < 1$). We observed that this mass compensation does not have a significant influence on the overall flow dynamics. The procedure is similar to that used by Bunner and Tryggvason (2002) for the front-tracking method, Fujita et al. (2015) for the level set method and Sun and Sakai (2016) for the IBM-VOF method. It is important to emphasize that all the validation/verification test cases presented in Section 4.1 have been simulated without such mass compensation and the maximum mass error is merely in the order of $10^{-3}\%$ relative to initial mass.

3.3.2. Computation of the volumetric surface tension force

In the density-scaled continuum surface force (CSF) model (Brackbill et al., 1992) the surface tension force acts via a source term $\mathbf{F}_\sigma$ in the momentum equation which only acts in the vicinity of the interface. The expression for $\mathbf{F}_\sigma$ is given by:

$$\mathbf{F}_\sigma = \frac{\rho}{\langle\rho\rangle}\sigma\kappa\mathbf{n} \tag{14}$$

where σ is the coefficient of surface tension, $\mathbf{n} = \nabla F$ is the interface normal vector and $\langle\rho\rangle$is the average density of the two fluid phases. The expression for the curvature κ is obtained from the divergence of the unit normal vector to the interface:

$$\kappa = -(\nabla\cdot\hat{\mathbf{n}}) = -\left(\nabla\cdot\frac{\mathbf{n}}{|\mathbf{n}|}\right) = \frac{1}{|\mathbf{n}|}\left[\frac{\mathbf{n}}{|\mathbf{n}|}\cdot\nabla|\mathbf{n}| - (\nabla\cdot\mathbf{n})\right] \tag{15}$$

The normal to the interface is actually computed from the gradient of the smoothed phase fraction $\widetilde{F}$. So, the formulas above hold with $\mathbf{n} = \nabla\widetilde{F}$. The smoothing technique used in this paper will be discussed in the next section. The density scaling used in the CSF model distributes the acceleration due to surface tension (i.e., $\mathbf{F}_\sigma/\rho$) symmetrically across the interface while conserving the total surface tension force. This improves the stability of the numerical model by reducing the parasitic currents (Yokoi, 2014) especially for the case when there is a high density ratio between the two fluid phases.

3.3.3. Smoothing of fluid phase fraction F

As indicated before, the interface orientation (i.e. the normal to the interface) is computed from the gradient of the fluid phase fraction F according to Eq. (13). Basically this involves numerical differentiation of a discontinuous function, leading to inaccuracies. This problem can be overcome by making use of a smoothed phase fraction $\widetilde{F}$ for the computation of the unit interface normal, i.e. using Eq. (13) with F replaced by $\widetilde{F}$ obtained from:

$$\widetilde{F}(x,y,z) = \sum_m D(x-x_m)D(y-y_m)D(z-z_m)F(x_m,y_m,z_m) \tag{16}$$

Here the smoothing function D is given by the polynomial expression proposed by Deen et al. (2004) as follows:

$$D(x) = \begin{cases} \frac{15}{16}\frac{1}{h}\left[\left(\frac{x}{h}\right)^4 - 2\left(\frac{x}{h}\right)^2 + 1\right], & |x| \leqslant h \\ 0, & |x| > h \end{cases} \tag{17}$$

where h represents the width of the computational stencil used for the smoothing. We typically use $h = 2\Delta$ where Δ is the Eulerian grid size, unless otherwise stated. The width of the computational stencil for the smoothing should be selected carefully. When the width is too small numerical instabilities may still arise, especially in the case where coefficient of surface tension is high. On the other hand when the width of the computational stencil is chosen too large, excessive smoothing (thickening) of the interface is obtained, which is undesirable.

In presence of immersed boundaries, the smoothing stencil used for the fluid-cells near a boundary may contain some solid-cells. However, solid-cells do not have any physical value of the fluid phase fraction F. To overcome this problem, F is extended in the solid region at any general contact angle using a method proposed by Sussman (2001). An 'extension' Eq. (18) in the form of advection Eq. (3) is solved for the solid region using an artificial extension velocity $\mathbf{u}^{\mathbf{extend}}$ and artificial timestep $\Delta\tau$. Note that this extension is carried out using the same pseudo-Lagrangian geometrical advection scheme used to advect F in the fluid region as described in Section 3.3.1.

$$\frac{\partial F}{\partial \tau} + \mathbf{u}^{\text{extend}} \cdot \nabla F = 0 \tag{18}$$

For all computations reported in this paper, extension is carried out up to 4 grid cells in the solid region using $\Delta\tau = 0.5\Delta$. Applying this method eliminates the need to modify the smoothing stencil for the fluid-cells near the immersed boundary while maintaining the continuity of $\widetilde{F}$ across it. For more clarification, Fig. 2(a)–(c) represents original fluid phase fraction F, extended fluid phase fraction and smoothed fluid phase fraction $\widetilde{F}$, respectively.

For the diffuse interface treatment of the immersed boundary (Sussman, 2001), this procedure would also apply the contact angle boundary condition as the fluid forcing is continuous and spread over few grid cells across the immersed boundary. So, fluid-cells near the boundary can experience the surface tension force due to the interface curvature (governed by extended and smoothed phase fraction $\widetilde{F}$) from solid region. However, in the present sharp IBM we have discontinuity at the immersed boundary between fluid and solid regions and hence contact angle boundary condition needs to be explicitly enforced as described in the subsequent section.

3.4. Contact line dynamics

In presence of a fluid-fluid interface with immersed solids, contact line dynamics plays a major role in wetting-dewetting phenomena. It can be easily incorporated in the current framework of CSF model by applying the appropriate contact angle boundary condition at contact lines. The contact angle may have a single value (static) or different values (dynamic) depending upon the local contact parameters and fluid properties. The effect of the contact angle is taken into account by modifying the interface normals at the solid boundaries as follows:

$$\hat{\mathbf{n}} = \hat{\mathbf{n}}_s \cos\theta + \hat{\mathbf{t}}_s \sin\theta \tag{19}$$

where θ is the contact angle, $\hat{\mathbf{n}}_s$ is the unit solid surface normal pointing inside the solid as seen from the fluid and $\hat{\mathbf{t}}_s$ is the unit tangent which lies on the solid surface and is normal to both $\hat{\mathbf{n}}_s$ and the contact line as shown in Fig. 3. $\hat{\mathbf{n}}_s$ can be easily found analytically for simple shapes such as spherical or cylindrical surface. For more complicated geometries it follows from the surface mesh that describes it or can be computed using the solid fraction as proposed by Washino et al. (2011). The tangential unit vector, $\hat{\mathbf{t}}_s$, can be found as

$$\hat{\mathbf{t}}_s = \frac{\nabla F - (\hat{\mathbf{n}}_s \cdot \nabla F)\hat{\mathbf{n}}_s}{|\nabla F - (\hat{\mathbf{n}}_s \cdot \nabla F)\hat{\mathbf{n}}_s|} \tag{20}$$

If one would have a body conformal grids, contact angle boundary condition could applied at all the cell vertices which are conformal with solid boundaries. For our case this holds for the outer boundaries of the computational domain. For a general immersed object its boundaries do not align with the Cartesian grid as shown

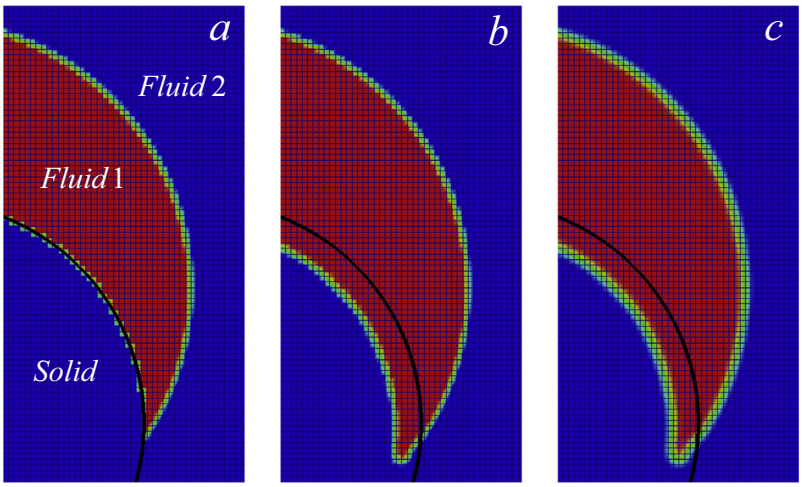

Fig. 2. Stepwise evolution of fluid phase fraction field: (a) Original fluid phase fraction F, (b) extended fluid phase fraction and (c) smoothed fluid phase fraction $\widetilde{F}$.

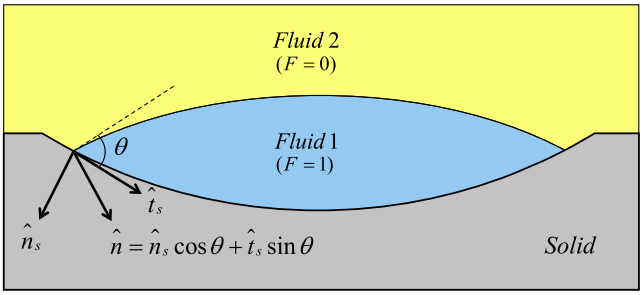

Fig. 3. Contact angle boundary condition implementation at solid boundaries. The fluid-fluid-solid contact line runs perpendicular to this figure.

in Fig. 1, In this case, the contact angle boundary condition is applied on all the vertices of the solid-cells which have at least one immediate neighbor in the fluid. In this way, the contact angle boundary condition is applied very close to the solid boundaries (if not exactly on it). Fig. 1 shows the solid-cell p has one of its neighbors q as a fluid-cell. So, the contact angle boundary condition is applied on all the vertices 1, 2, 3 and 4 of the solid-cell p.

Contact line dynamics is a molecular phenomenon, which suggests that the macroscopic flow can be strongly affected by interactions at molecular scales between fluids and solid substrate (Snoeijer and Andreotti, 2013). It is essential to take into account the effect of this sub-grid phenomenon for macroscopic-grid modeling. Different theoretical and experimentally inspired models are available in the literature (consolidated by Saha and Mitra (2009)) and they differ in the approach taken to connect the molecular and macroscopic length scales.

Apart from molecular scale phenomena, the flow field varies significantly on small (but macroscopic) distances from the contact line. When using a large grid size the flow field near the contact line is under resolved and also hydrodynamic phenomena should be accounted for in the model for the contact line dynamics. As we are interested in flows in complex porous geometries with low Reynolds Re and capillary Ca numbers, a model developed by Voinov (1976) and Cox (1986) has been adopted which links the dynamic contact angle θ_d with equilibrium contact angle θ_e using a slip length λ and slip capillary number Ca_{cl} as follows:

$$\begin{aligned}
&\theta_d^3 = \theta_e^3 + 9\,\text{sgn}_{\text{dir}}\, Ca_{\text{cl}} \ln\left(\frac{L}{\lambda}\right) \text{with} \\
&Ca_{\text{cl}} = \frac{\mu |\mathbf{U}_{\text{cl}}|}{\sigma}, \\
&\mathbf{U}_{\text{cl}} = (\mathbf{u}_{\text{cl}} \cdot \hat{\mathbf{t}}_s) \frac{\hat{\mathbf{t}}_s}{|\hat{\mathbf{t}}_s|} \text{and} \\
&\text{sgn}_{\text{dir}} = -\text{sign}(\mathbf{U}_{\text{cl}} \cdot \hat{\mathbf{n}})
\end{aligned} \tag{21}$$

where $|\mathbf{U}_{\text{cl}}|$ is contact line velocity, i.e., the magnitude of the slip velocity parallel to the tangent direction $\hat{\mathbf{t}}_s$ which is found out using a density weighted average velocity $\mathbf{u}_{\text{cl}}$ of the fluid nodes in the vicinity of the contact line. sgn_{dir} signifies the direction of the contact line motion, with: $\text{sgn}_{\text{dir}} = +1$ or -1 for advancing and receding contact lines, respectively. L is the macroscopic or grid length scale. For the slip length λ, as observed by Lauga et al. (2007), we have taken a fixed value of $\lambda = 10^{-9}$m in Eq. (21) for all the simulations reported in this paper.

4. Results

4.1. Verification and validation

The IBM implementation has been thoroughly tested by Das et al. (2017) for various cases. They validated their simulations with existing numerical and/or experimental results from literature. In 2D, they have considered a case of flow past a cylinder and validation has been performed for the non-dimensional drag and lift forces, unsteady vortex shedding frequency and length of the recirculation zone. In 3D, the case of flow past a sphere has been validated by comparing the non-dimensional drag force for Reynolds numbers as high as 500. Implicit implementation of the periodic boundary conditions for IBM has been validated for the case of flow past a simple cubic (SC) array of spheres by comparing the non-dimensional drag force for the Stokes flow regime with two different porosities. The IBM was found to be 2nd order accurate with an error less than 2% for 15 cells across the sphere diameter. They have also simulated the flow through periodic complex porous structures, i.e. an open cell foam for a wide range of porosities, and compared the obtained results with the well-known Carman-Kozeny and Ergun correlations.

Van Sint Annaland et al. (2005) did an extensive validation of their 3D VOF model, starting from basic problems such as advection tests and the Laplace pressure difference across a curved fluid-fluid interface. They also investigated gas bubbles rising in quiescent viscous liquids and computed the terminal rise velocity and the shape of the rising bubble for high density and viscosity ratios. The obtained results agreed very well with the Grace diagram for a very wide range of Eötvös and Morton numbers. They also tested their model successfully for cases where the interface experiences substantial deformation, i.e. co-axial and oblique coalescence of two gas bubbles rising in a viscous liquid, and obtained good agreement with experimental results published in literature. Baltussen et al. (2014) performed bubble advection test with 30 grid cells across the bubble diameter and found the global mass error to be negligible ($10^{-7}\%$).

In this section we present verification/validation test cases for the 3D VOF with contact line dynamics, both with and without IBM. To test the static contact angle boundary condition two problems are investigated: (i) the equilibrium shape of a droplet on a flat surface and (ii) the equilibrium shape of a droplet on a spherical surface. The simulations are compared with known analytical expressions. To check the dynamic contact angle boundary condition we investigate the problem of droplet spreading on a flat surface and compare the temporal evolution of dimensionless droplet contact radius with experimental and other numerical results available in literature. A grid dependence study for the same test case is shown in Appendix A. As our interest lies in oil-water flows through complex structures, oil-water systems are used for these simulations by default, unless otherwise specified. For all simulations reported in this paper, the time step Δt has been chosen such that it satisfies both Courant-Friedrichs-Lewy (CFL) and capillary criteria as follows:

$$\begin{aligned}
&\Delta t < \Delta t_{\text{CFL}} = \frac{\Delta}{U_{\max}} \\
&\Delta t < \Delta t_{\sigma} = \sqrt{\frac{(\rho_1 + \rho_2)\Delta^3}{4\pi\sigma}}
\end{aligned} \tag{22}$$

Here, Δt_{CFL} and Δt_{σ} are the minimum required time steps according to the CFL and capillary criteria, respectively. Δ is the computational grid size and $U_{\max}$ is the maximum fluid velocity in the computational domain.

4.1.1. Equilibrium shape of a droplet on a flat surface

In this section, we investigate the equilibrium shape of an oil droplet in water on a flat surface with static contact angle θ_s. Physical properties of an oil-water system used for the simulations are as follows: water density $\rho_w = 1000$ kg/m^3, water dynamic viscosity $\mu_w = 0.001$ Pa s, oil density $\rho_o = 950$kg/m^3, oil dynamic viscos-

ity $\mu_o = 0.02$ Pa s and coefficient of surface tension $\sigma = 0.03$ N/m. The Eötvös number Eo, defined with respect to initial droplet radius R_0, has been used to quantify the relative effect of gravitational force compared to surface tension force:

$$Eo = \frac{(\rho_w - \rho_o) g R_0^2}{\sigma} \tag{23}$$

First, simulations are performed for the case where gravity is absent ($Eo = 0$). Initially, the droplet is placed in the computational domain such that its center is at the distance equal to the initial droplet radius R_0 from the flat surface. In this condition, the droplet will just touch the flat surface. As the initial contact angle is different from the static contact angle, the droplet will spread until it reaches equilibrium. Schematic diagrams of the initial and equilibrium droplet shapes are presented in Fig. 4. All the geometrical and computational parameters used for the simulations are listed in Table 1. No-slip boundary conditions are applied at all computational domain boundaries. Note that the contact angle boundary condition is applied without the use of IBM, because the contact line is located on the lower (flat) boundary of the computational domain. As the total drop volume $V = \frac{4}{3}\pi R_0^3$ is constant, all equilibrium shape parameters such as droplet contact radius r_f, radius of curvature R_f and height h_f can be derived analytically according to the following relations:

$$V = \frac{4}{3}\pi R_0^3 = \pi R_f^3 \left(\frac{2}{3} - \cos\theta_s + \frac{1}{3}\cos^3\theta_s\right) \tag{24}$$

$$h_f = R_f(1 - \cos\theta_s) \tag{25}$$

$$r_f = R_f \sin\theta_s \tag{26}$$

The droplet height h_f and contact radius r_f for the equilibrium shape have been found numerically and compared with the analytical results of Eqs. (25) and (26), respectively. The obtained numerical results show an excellent match with the analytical results, as shown in Fig. 5. The numerical and analytical equilibrium droplet shapes are compared in Fig. 6 which shows very satisfactory qualitative matching. Note that the numerical profiles are generated by computing the iso-contours of the smoothed phase fraction $\widetilde{F} = 0.5$. The quantitative error in equilibrium droplet shape is defined by the mean difference as follows:

$$E = \frac{1}{N}\sum_{i=1}^{N} \frac{|y_i^{\widetilde{F}=0.5} - y_i^{\text{analytical}}|}{R_f} \tag{27}$$

where N is the number of points discretizing the interface. $y_i^{\widetilde{F}=0.5}$ and $y_i^{\text{analytical}}$ the are numerical and analytical y-coordinate of the interface point whose x-coordinate is $x_i^{\widetilde{F}=0.5}$. For the shapes shown in Fig. 6, the mean differences are 0.69%, 0.36%, 0.33%, 0.49% and 2.76% for $\theta_s = 30^\circ, 60^\circ, 90^\circ, 120^\circ$ and 150° respectively.

As the CSF model distributes the volumetric surface tension force smoothly across the interface as per Eq. (14), one would expect the pressure distribution also to be smooth. However, in reality, a droplet would experience the Laplace pressure difference $\Delta P_{\text{analytical}} = \frac{2\sigma}{R_f}$ (in 3D) as a step function across the interface (at least at macroscopic scales). The expected value of $\Delta P_{\text{analytical}}$ is compared with the numerical pressure difference (Fig. 7), evaluated in three different ways:

1. ΔP_0: Pressure difference between the center of the droplet and boundaries of the simulation domain. This totally eliminates the effect of the interface distribution, because interface cells are excluded from the calculation.

Table 1
Geometrical and computational parameters used for the simulations of equilibrium shape of a droplet on a flat surface without gravity ($Eo = 0$).

Parameter	Value	Unit
Computational grid (n_x, n_y, n_z)	(120,60,120)	Cell
Grid size (Δ)	5×10^{-5}	m
Timestep (Δt)	10^{-5}	s
Droplet initial radius (R_0)	0.001	m
Droplet initial position (x_0, y_0, z_0)	(0.003,0.001,0.003)	m
Static contact angle (θ_s)	30, 60, 90, 120, 150	°

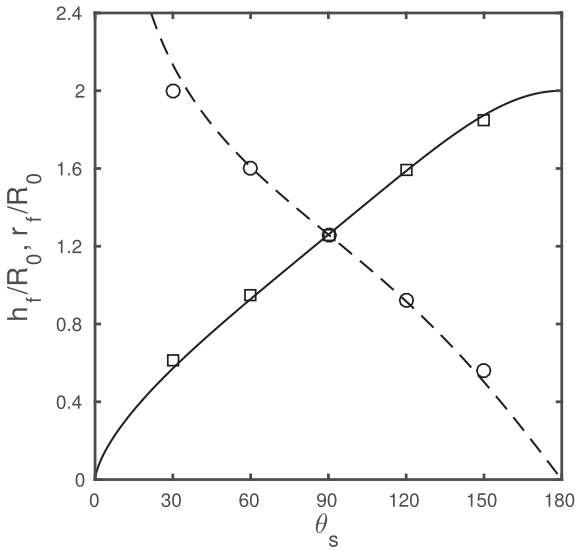

Fig. 5. Dimensionless droplet parameters for the equilibrium shape of a droplet on a flat surface without gravity ($Eo = 0$): analytical height (–), numerical height (□), analytical contact radius (– –), numerical contact radius (◯).

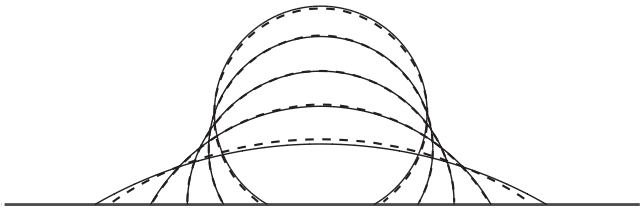

Fig. 6. Analytical (–) and numerical (– –) equilibrium droplet shapes on a flat surface without gravity ($Eo = 0$) for static contact angles θ_s = 30°, 60°, 90°, 120° and 150°.

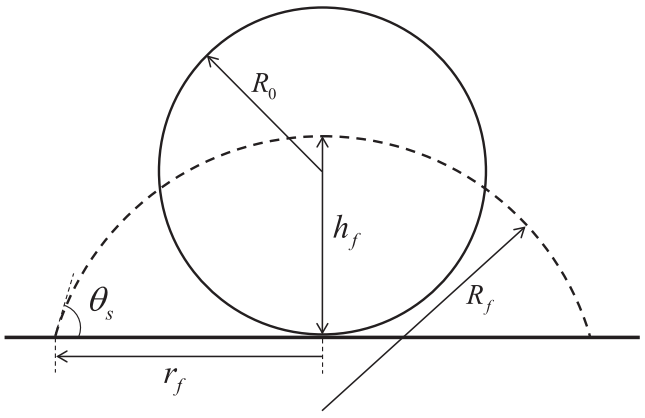

Fig. 4. Schematic representation of the initial (–) and equilibrium (– –) shapes of the a droplet on a flat surface with static contact angle without gravity ($Eo = 0$).

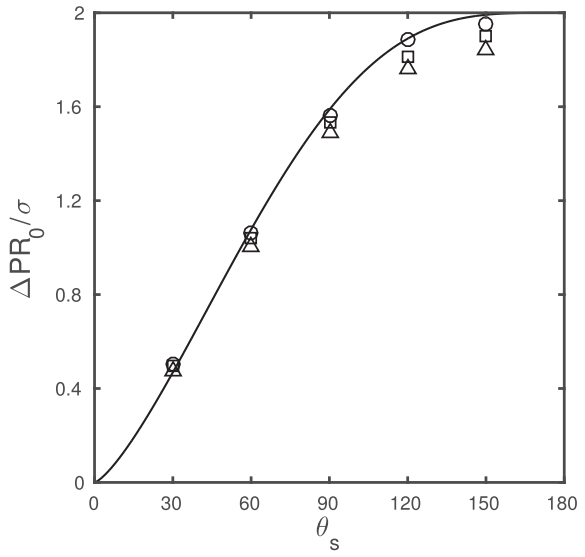

Fig. 7. Dimensionless pressure difference for a droplet on a flat surface in equilibrium without gravity ($Eo = 0$) : $\Delta P_{\text{analytical}}$ (–), ΔP_0 (○), $\Delta P_{\text{partial}}$ (□) and ΔP_{total} (Δ).

2. $\Delta P_{\text{partial}}$: Average pressure difference between the computational cells in regions for which $0.95 \leqslant F \leqslant 1.0$ and regions for which $0.0 \leqslant F \leqslant 0.05$. This will only have a partial effect of the interface distribution, because most of the interface cells ($0.05 < F < 0.95$) are excluded from the calculation.
3. ΔP_{total}: Average pressure difference between the computational cells in regions for which $0.5 \leqslant F \leqslant 1.0$ and regions for which $0.0 \leqslant F \leqslant 0.5$. This will have the full effect of the interface distribution, because all interface cells are included in the calculation.

There are two main sources of error in the numerical calculation of the pressure difference across the interface: (i) Error due to the inaccuracy in numerical value of R_f. Fig. 6 qualitatively shows that this error is highest in the case of $\theta_s = 30^\circ$ and (ii) as pressure varies smoothly across the interface, inclusion of computational cells from and near the interface in the calculation would reduce the numerical pressure difference across the interface. Fig. 7 reports on this behavior with $\Delta P_0 > \Delta P_{\text{partial}} > \Delta P_{\text{total}}$.

Last, we present the simulations to compute the equilibrium droplet shapes under the influence of gravity ($Eo > 0$). Simulations have been performed for static contact angle $\theta_s = 120^\circ$ for a wide range of Eötvös numbers. The analytical equilibrium droplet shape for $\theta_s = 120^\circ$ without gravity (shown in Fig. 6) is taken as initial condition to reduce the computation time. The computational domain is divided in $(n_x, n_y, n_z) = (300, 80, 300)$ grid cells in x, y and z direction, respectively, with a grid size $\Delta = 2.5 \times 10^{-5}$ m. Simulations have been performed with a time step $\Delta t = 5 \times 10^{-6}$ s. No-slip boundary conditions are applied at all computational domain boundaries. At lower Eötvös numbers ($Eo \ll 1$) the droplet maintains its original spherical cap shape as the surface tension forces are dominant and the droplet height in this case is controlled by Eq. (25). At higher Eötvös numbers ($Eo \gg 1$) the droplet forms a puddle under the influence of gravity whose height is proportional to the capillary length scale and given by the following expression:

$$h_\infty = 2\sqrt{\frac{\sigma}{(\rho_w - \rho_o)g}}\sin\left(\frac{\theta_s}{2}\right) \tag{28}$$

Fig. 8 shows the equilibrium droplet shapes and dimensionless droplet height (h^*) for a wide range of Eötvös numbers. h^* is defined as the ratio of the droplet height for a given Eötvös number to the droplet height without gravity ($Eo = 0$) given by Eq. (25). The obtained results show an excellent agreement with two asymptotic solutions given by Eqs. (25) and (28). As expected, the transition between spherical cap and puddle is observed at $Eo \sim 1$.

4.1.2. Equilibrium shape of a droplet on a spherical surface

In this section, we simulate the equilibrium shapes of an oil droplet in water on a spherical surface with different static contact angles θ_s. The influence of gravity is not taken into account. The physical properties of the oil-water system are the same as used in Section 4.1.1. The radius of the solid sphere is the same as the initial radius of the droplet R_0.

Initially, the droplet is placed in the computational domain such that its center is at a distance equal to R_0 from the spherical surface. In this condition, the droplet will just touch the spherical surface. As the initial contact angle is different from the static contact angle, the droplet will spread until it reaches equilibrium. Schematic diagrams of the initial and equilibrium droplet shapes are presented in Fig. 9. As the total drop volume $V = \frac{4}{3}\pi R_0^3$ is constant, the final equilibrium shape can be derived analytically by solving the following nonlinear equations:

$$\alpha + \beta = \theta_s \tag{29}$$

$$r_f = R_f \sin\beta = R_0 \sin\alpha \tag{30}$$

$$\frac{\pi R_f^3}{3}(1+\cos\beta)^2(2-\cos\beta) + \frac{\pi R_0^3}{3}(1+\cos\alpha)^2(2-\cos\alpha) - \frac{4\pi R_0^3}{3} = \frac{4\pi R_0^3}{3} \tag{31}$$

All the geometrical and computational parameters used for the simulations are listed in Table 2. Note that the contact line moves on the spherical surface which is modeled as an immersed boundary. Therefore the IBM implementation of the contact angle boundary condition is applied here. No-slip boundary conditions are applied at all computational domain boundaries as well as at the solid sphere boundary. Numerical and analytical equilibrium droplet shapes are presented in Fig. 10, which shows an excellent

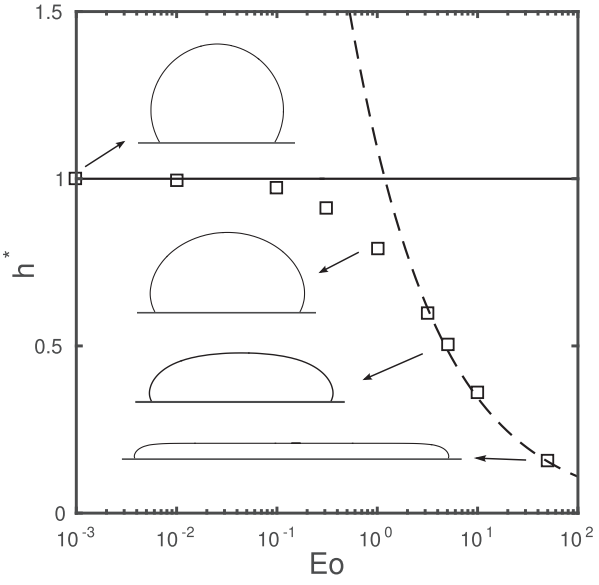

Fig. 8. Equilibrium droplet shapes and dimensionless droplet height (h^*) on a flat surface with Eötvös number: numerical results (□), asymptotic solutions of Eq. (25) (–) and Eq. (28) (– –).

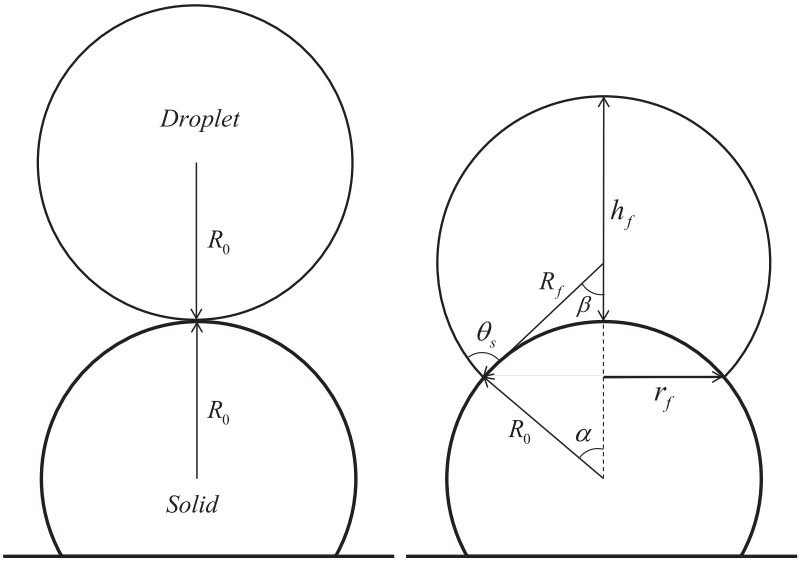

Fig. 9. Schematic representation of the initial (left) and equilibrium (right) shapes of the a droplet on a spherical surface with static contact angle.

Table 2
Geometrical and computational parameters used for the simulations of equilibrium shape of a droplet on a spherical surface.

Parameter	Value	Unit
Computational grid (n_x, n_y, n_z)	(80,80,80)	cell
Grid size (Δ)	5×10^{-5}	m
Time step (Δt)	10^{-5}	s
Droplet initial radius (R_0)	0.001	m
Droplet initial position (x_0, y_0, z_0)	(0.002,0.0025,0.002)	m
Solid sphere position (x_s, y_s, z_s)	(0.002,0.0005,0.002)	m
Static contact angle (θ_s)	30, 60, 90, 120, 150	°

qualitative match. Mean differences in equilibrium droplet shape, defined by Eq. (27), are 1.35%, 1.03%, 0.78%, 0.57% and 1.57% for $\theta_s = 30^\circ, 60^\circ, 90^\circ, 120^\circ$ and 150°, respectively.

The contact radius r_f and the droplet height h_f for the equilibrium shape have been found numerically and compared with analytical results of Eq. (30) and

$$h_f = R_f(1 + \cos\beta) - R_0(1 - \cos\alpha) \tag{32}$$

respectively. The obtained numerical results have an excellent match with the analytical results, as shown in Fig. 11. This validates the coupled IBM-VOF implementation for static contact angles.

4.1.3. Droplet spreading on a flat surface

In this section, we simulate the transient behavior of a squalene oil droplet in air spreading on a flat surface with a dynamic contact angle. Physical properties used for the simulations are: squalene oil density $\rho_{sq} = 809\ \text{kg/m}^3$, squalene oil dynamic viscosity $\mu_{sq} = 0.034$ Pa s, air density $\rho_a = 1.2\ \text{kg/m}^3$, air dynamic viscosity $\mu_a = 2 \times 10^{-5}$ Pa s and air-oil surface tension $\sigma = 0.032$ N/m. Initially, a droplet with radius $R_0 = 0.001$ m is placed on a flat surface such that its center is at the height $h = 0.95R_0$ from the flat surface. In this condition it has an initial contact radius of r_0 with the flat surface. The droplet will spread with dynamic contact angle θ_d until it reaches the equilibrium contact angle θ_e with the flat surface and in this condition the final contact radius is r_f. Schematic diagrams of the initial and equilibrium droplet states are presented in Fig. 12. Simulations have been performed in absence of gravity with a grid

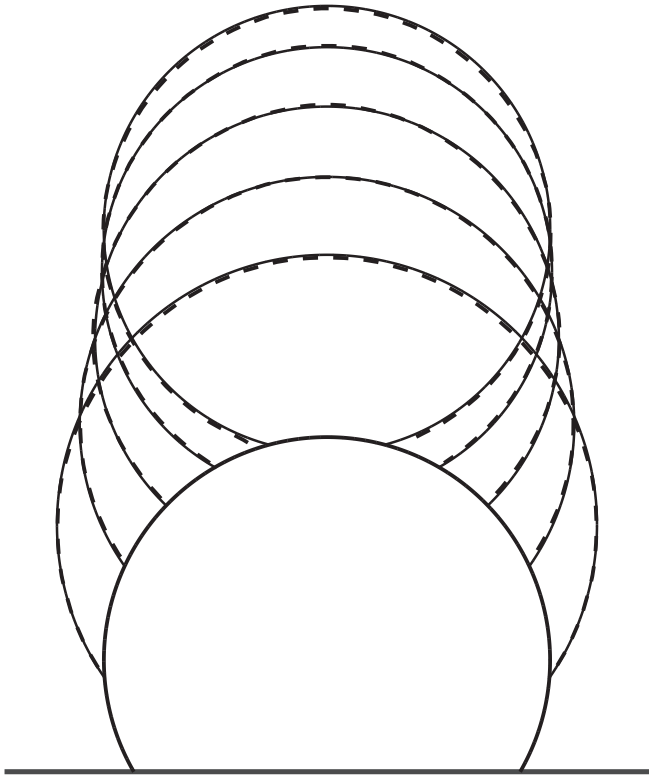

Fig. 10. Analytical (–) and numerical (– –) equilibrium droplet shapes on a spherical surface for static contact angles θ_s = 30°, 60°, 90°, 120° and 150°.

size $\Delta = 5 \times 10^{-5}$ m and time step $\Delta t = 5 \times 10^{-7}$ s. The Cox and Voinov model, given by Eq. (21), has been used to calculate the local θ_d using the value of $\theta_e = 41.5^\circ$.

Lavi and Marmur (2004) performed experiments for different liquids (including squalene oil) droplets spreading on a coated silicon wafer and gave the following relation for the temporal evolution of the contact area:

$$\frac{A(\tau)}{A_f} = 1 - \exp\left[-\frac{K}{A_f}\tau^m\right] \tag{33}$$

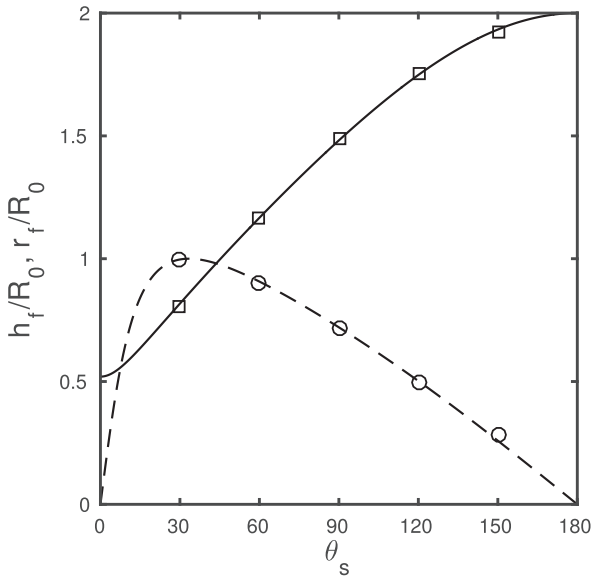

Fig. 11. Dimensionless droplet parameters for the equilibrium shape of a droplet on a spherical surface: analytical height (–), numerical height (□), analytical contact radius (– –), numerical contact radius (○).

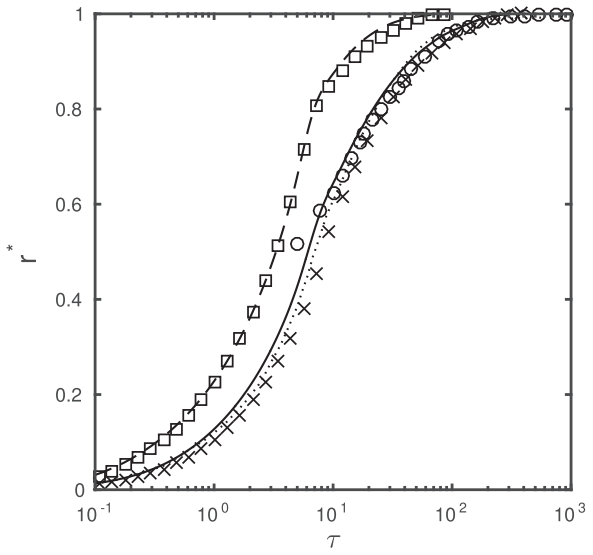

Fig. 13. Dimensionless contact radius r^* with dimensionless time τ for Dynamic contact angle: present without IBM (–), present with IBM (×), experiments by Lavi and Marmur (2004) (○), simulations by Legendre and Maglio (2015) (· · ·) and Static contact angle: present without IBM (– –), present with IBM (□).

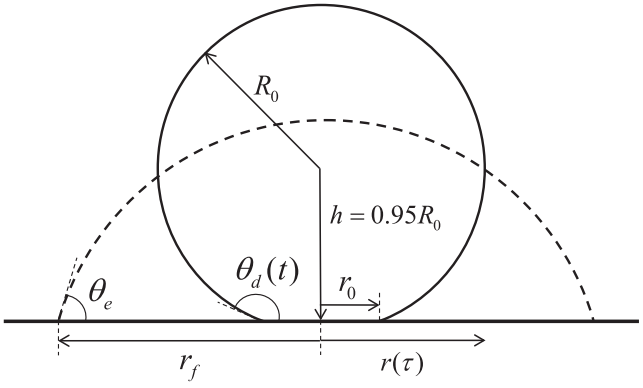

Fig. 12. Schematic representation of the initial (–) and equilibrium (– –) states of the a droplet spreading on a flat surface with dynamic contact angle.

where A_f is the final value of the contact area, $A(\tau)$ is the contact area at dimensionless time $\tau = \sigma t/(\mu_{sq} V^{\frac{1}{3}})$, and K and m are fitting parameters which depend on the spreading liquid. Legendre and Maglio (2015) performed 2D axisymmetric VOF simulations for the same test case with different h values ($0.99R_0, 0.98R_0$ and $0.95R_0$) and showed that the droplet spreading is independent of its initial position for dimensionless contact radius r^* defined as:

$$r^* = \frac{r(\tau) - r_0}{r_f - r_0} \tag{34}$$

In the present simulations, a flat surface is defined in two different ways: (i) as a body conformal computational domain boundary where the IBM implementation is not used, and (ii) as a non-body conformal IB plane passing though the computational domain where the IBM implementation is used to apply contact angle boundary condition.

Fig. 13 shows the temporal evolution of r^* with τ for both cases with static and dynamic contact angles. The obtained results are compared with the experimental results of Lavi and Marmur (2004) and numerical results of Legendre and Maglio (2015). A significant difference has been observed between the spreading with dynamic and static contact angles. The total dimensionless spreading time for a dynamic contact angle is almost four times that for a static contact angle. The obtained results with a dynamic contact angle show a very satisfactory match with the results reported in literature. Note that there is a very small difference between the obtained results with and without IBM implementation for a static contact angle, while this difference is somewhat higher in the case of a dynamic contact angle. The reason is that spreading with a dynamic contact angle is greatly influenced by the magnitude of the contact line velocity $|\mathbf{U}_{cl}|$ according to Eq. (21), and the numerical calculation of $|\mathbf{U}_{cl}|$ is more accurate on body conformal grids compared to non-body conformal grids.

For the present simulations with IBM, capillary number based on the maximum magnitude of the spurious velocity in steady state is less than 2×10^{-3}. It is in the same order as reported by Baltussen et al. (2014) for the stationary bubble test case (without IBM). So, the presence of immersed solid boundaries doesn't change the order of spurious velocities in the current coupled IBM-VOF implementation.

4.2. Water flooding simulations

In this section, we present pore-scale simulations of a water flooding process such as encountered in enhanced oil recovery. Flooding simulations of periodic body centered cubic (BCC) and face centered cubic (FCC) structures showcase the capabilities of the present method.

The physical properties of an oil-water system are same as in Section 4.1.1. Initially the BCC and FCC structures are fully saturated with oil, as shown in Fig. 14. Flow parameters are chosen such that the Reynolds number $Re = \rho_o U_{in} D/\mu_o$ and capillary number $Ca = \mu_o U_{in}/\sigma$ defined with respect to the sphere diameter D and water inlet velocity U_{in} are 1 and 0.01, respectively. A neutral (90°) static contact angle is used at the three phase contact line. Inlet and outlet boundary conditions are applied in the flow (x) direction and periodic boundary conditions are applied in the cross-flow (y and z) directions. The domain size for BCC and FCC structures are $(n_x, n_y, n_z) = (240, 60, 60)$ and $(288, 72, 72)$, respectively, and chosen such that the number of grid cells across a sphere radius R is at least 25.

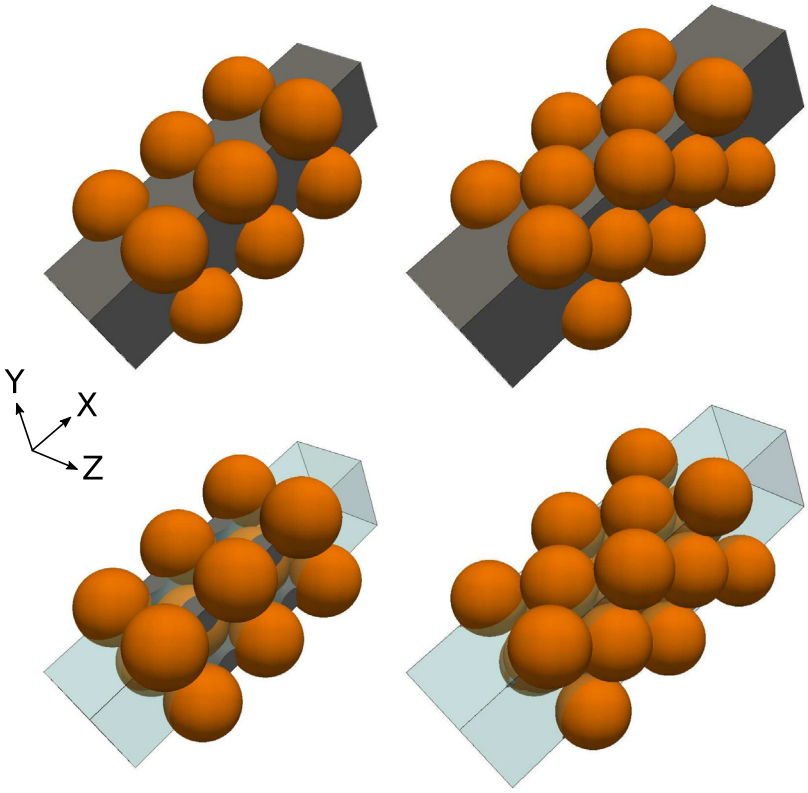

Fig. 14. Initial (top) and steady state (bottom) conditions for the pore-scale water flooding process through periodic BCC (left) and FCC (right) structures. Oil, water and solid spheres are represented by gray, transparent blue and brown color respectively. (For interpretation of the references to color in this figure legend, the reader is referred to the web version of this article.)

Oil from the pores will be displaced as the inlet water front progresses and penetrates into the pores. The Simulations have been performed until a steady state is achieved. Fig. 14 shows the residual oil in the pores after the water flooding process through both BCC and FCC structures.

To characterize the pore-scale water flooding process in detail, the amount of residual oil present in the porous bed is plotted as a function of dimensionless time τ in Fig. 15. For this graph we use a representative fluid volume in the center of each bed that we will refer to as the 'pore' below (indicated in Fig. 16). The dimensionless time is defined as: $\tau = (t - t_0)/T$, where t_0 is the time when water front enters the pore and $T = V_{\text{pore}}/Q$ is the residence time scale with V_{pore} and Q are the pore volume and volumetric flow rate, respectively. Note that V_{pore} for the BCC and FCC structure is $\left(\frac{8}{3\sqrt{3}} - \frac{\pi}{3}\right)D^3 \approx 0.4924D^3$ and $\left(\sqrt{8} - \frac{2\pi}{3}\right)D^3 \approx 0.7340D^3$, respectively.

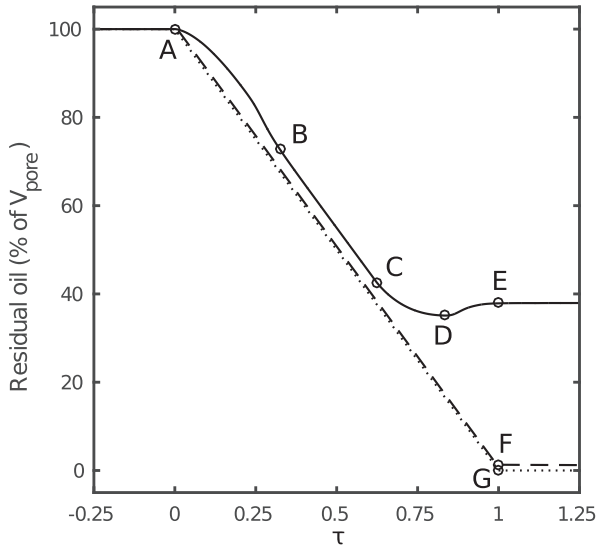

Fig. 15. Residual oil in the pore as a percentage of V_{pore} with τ for periodic BCC (–) and FCC (– –) structures. Dotted line (···) represents the ideal (piston-like) recovery.

As shown in Fig. 15, the line *AG* represents the case where all the pore oil is displaced by the incoming water. This type of oil recovery is called ideal or piston-like recovery. In case of the FCC structure, the oil recovery plot *AF* almost coincides with the line *AG* and hence we observe almost piston-like oil recovery for the FCC structure with residual oil amounting to only 1.33% of V_{pore}. However, in the case of the BCC structure, the oil recovery plot *ABCDE* is a blend of a few different processes. Segments *AB* and *CD* are not parallel to the ideal recovery line *AG*, which suggests that some amount of oil remains in the pore during *AB* and *CD*. For a brief period during *BC*, the slope is almost parallel to line *AG* which shows that the oil recovery process during *BC* is almost piston-like. The amount of oil in the BCC pore increases slightly through *DE* which corresponds to the retracement of oil from surroundings into the pore. The residual oil in the BCC pore is 38.01% of V_{pore} at the end of the recovery process. For extra clarification, Fig. 16 shows subsequent images of the pore-scale water flooding process for the BCC and FCC structures at $\tau = 0, 0.25, 0.5, 0.75$ and 1. Note that the oil-water interface makes 90° contact angle with the solid surface in all images.

The packing factors of BCC and FCC structures are $\frac{\pi\sqrt{3}}{8} \approx 0.6802$ and $\frac{\pi}{3\sqrt{2}} \approx 0.7404$, respectively. Moreover, the number of solid spheres per pore are 2 and 4 for BCC and FCC structures respec-

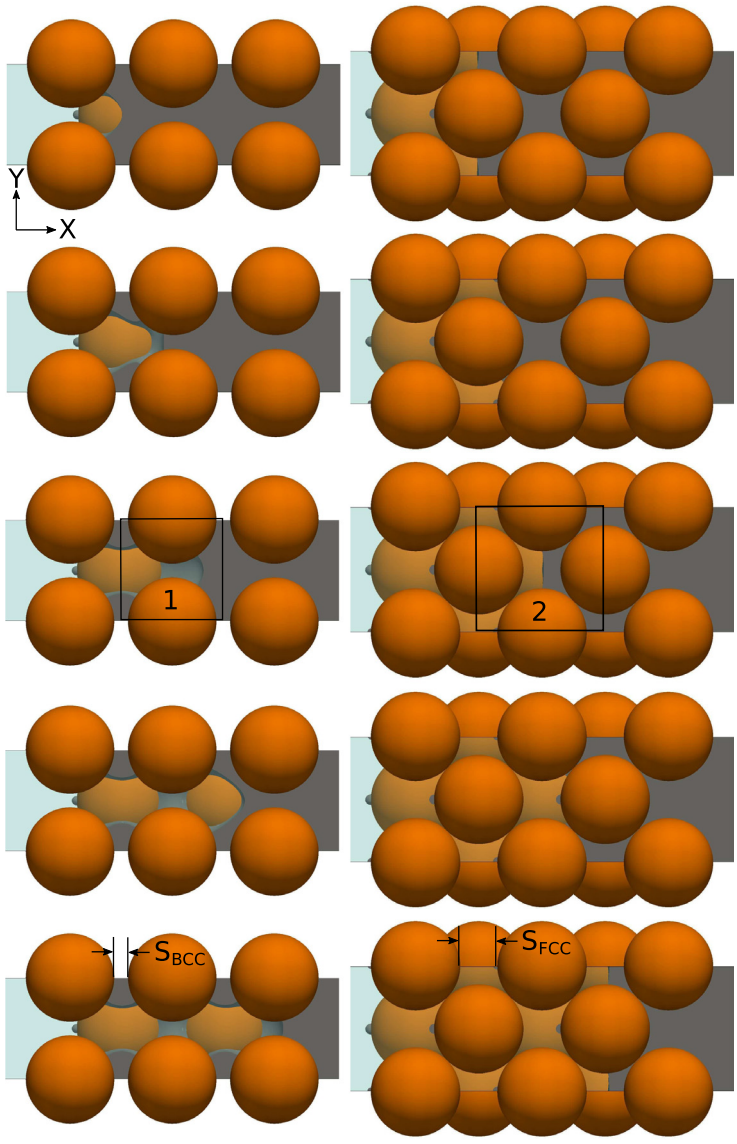

Fig. 16. Pore-scale water flooding process for BCC (left) and FCC (right) structures at τ = 0, 0.25, 0.5, 0.75 and 1 (from top to bottom). 1 and 2 are BCC and FCC pores used for calculation of residual oil. S_{BCC} and S_{FCC} are the minimum pore gap in flow direction for BCC and FCC structures respectively.

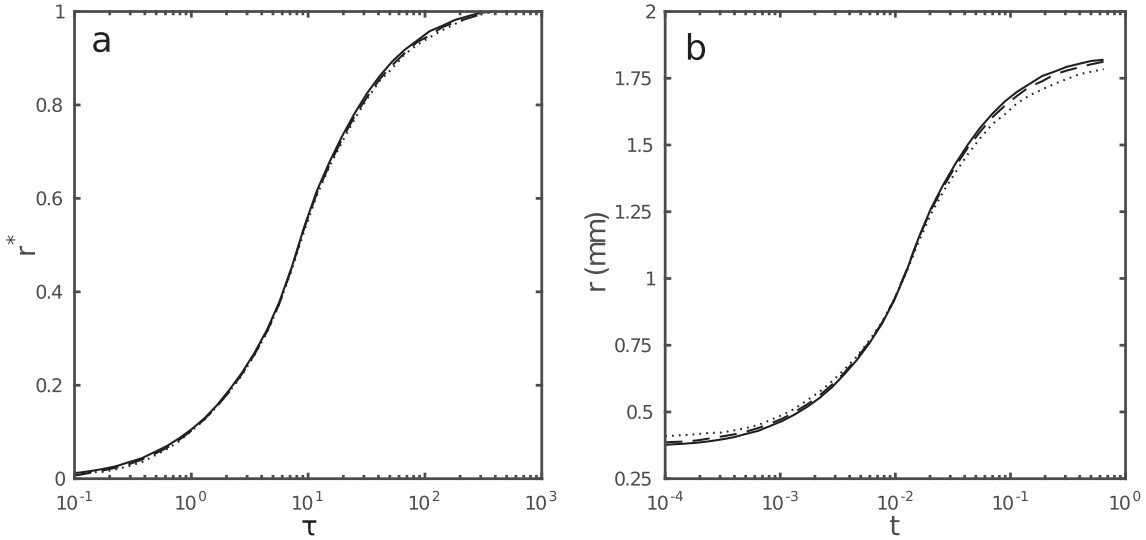

Fig. 17. Grid dependence study for the test case of a droplet spreading on a flat surface (generated by IB plane) with dynamic contact angle: (a) Dimensionless contact radius r^* with dimensionless time τ and (b) Contact radius r with time t for different grid resolutions $G1$ (···), $G2$ (– –) and $G3$ (–).

tively. So, FCC has a higher solid volume and twice the surface area per pore compared to the BCC structure. Thus, one might reason that the residual oil in case of FCC would be higher than BCC. However, the opposite behavior is observed, with the FCC structure showing almost a piston-like recovery whereas the residual oil for BCC is 38.01% of V_{pore}. The main reason for this behavior is the difference in the minimum gap between spheres in the flow direction for the BCC (S_{BCC}) and FCC (S_{FCC}) structures, as shown in Fig. 16. This gap will govern the strength of the local velocity field in the pore and its higher value suggests a stronger local velocity in the pore. In case of higher local velocity, oil is less likely to be held within the pore. From a geometric calculation it can be shown that $S_{BCC} = \left(\frac{2}{\sqrt{3}} - 1\right)D \approx 0.1547D$ and $S_{FCC} = \left(\sqrt{2} - 1\right)D \approx 0.4142D$. As S_{FCC} is quite high compared to S_{BCC}, the water from the surrounding penetrates easily into the FCC pore compared to BCC and hence oil recovery is higher for FCC than BCC structure.

It is also important to understand that S_{FCC} and S_{BCC} are dependent on the flow direction and for a different flow direction than the present case residual oil would be different. Thus, the pore-scale oil recovery is dependent on the flow direction. However, for large heterogeneous porous media (which oil reservoirs generally are) this directional effect would be statistically neutralized.

5. Conclusions

In this paper, a novel methodology is presented to numerically simulate multiphase flows through complex geometries, employing a finite volume methodology on a staggered grid. A second order, implicit, direct forcing and sharp interface immersed boundary method (IBM) is used to resolve the complex solid structure on a non-body conformal Cartesian computational grid. The fluid-fluid interface is tracked by a sharp interface and mass conservative volume of fluid (VOF) method. The volumetric surface tension force is numerically calculated using the continuum surface force (CSF) model, which is picked because of its simplicity and robustness especially with complex solid boundaries. Density scaling is used with the CSF model to reduce the parasitic currents. An apparent contact angle (static or dynamic) is applied as a boundary condition at the three-phase contact line in this coupled VOF-IBM framework to effectively reproduce contact line dynamics at macroscopic length scale.

Different test cases involving static and dynamic contact angles are simulated to validate the developed methodology. Simulation results match quite well with those obtained analytically or from literature. Pore-scale simulations of the water flooding process used for enhanced oil recovery (EOR) have been performed. The dynamics of oil-water flow through periodic body centered cubic (BCC) and face centered cubic (FCC) structures are simulated and the amount of residual oil is estimated. The present work provides a framework to further investigate the effect of Reynolds number, capillary number, contact angle/wettability, viscosity ratio, porosity etc. on the water flooding process. The developed methodology can also be extended for other EOR processes e.g. polymer or chemical flooding through complex porous structures.

Acknowledgments

This work is part of the Industrial Partnership Program (IPP) 'Computational sciences for energy research' of the Foundation for Fundamental Research on Matter (FOM), which is part of the Netherlands Organization for Scientific Research (NWO). This research program is co-financed by Shell Global Solutions International B.V.

Appendix A. Grid dependence study

A grid dependence study has been performed for the most complex test case: temporal evolution of a droplet spreading on a flat surface with dynamic contact angle presented in Section 4.1.3. Here, a flat surface generated by a non-body conformal IB plane is considered to test the coupled VOF-IBM implementation. Three different grid resolutions, $G1$ ($50 \times 50 \times 50$), $G2$ ($75 \times 75 \times 75$) and $G3$ ($100 \times 100 \times 100$) are investigated, each corresponding to a number of grid cells across R_0 equal to 10, 15 and 20, respectively. All other physical and computational parameters are kept constant for all cases. Fig. 17(a) shows the temporal evolution of dimensionless contact radius r^* with dimensionless time τ, whereas Fig. 17(b) represents the same in dimensional form as contact radius r with time t. All grid resolutions produce almost overlapping results in the dimensionless form where r^* is normalized using r_0 and r_f as specified in Eq. (34). However, the difference due to grid resolution is appreciable when the same quantities are plotted in dimensional form. The L^2 relative error norm (defined with respect to the finest grid G3) is used to quantify this difference as follows:

$$L^2 = \sqrt{\frac{\sum_{i=1}^{N}\left(r_{G3,i} - r_{G,i}\right)^2}{\sum_{i=1}^{N} r_{G3,i}^2}} \tag{35}$$

where G stands for the grids $G1$ or $G2$, i is the index to represent ith sampling point and N is total number of sampling points. Note that the sampling points are chosen on logarithmic scale as droplet spreading is governed by the exponential Eq. (33). Calculated L^2 relative error norms for grids $G1$ and $G2$ are 2.56% and 0.86%, respectively which shows that the grid $G2$ is good enough to produce accurate results. So, all the simulations reported in this paper use a number of grid cells across R_0 greater than or equal to 15.

References

Alvarado, V., Manrique, E., 2010. Enhanced oil recovery: an update review. Energies 3 (9), 1529–1575.
Herskowitz, M., Smith, J., 1983. Trickle-bed reactors: a review. AIChE J. 29 (1), 1–18.
Stone, H.A., Stroock, A.D., Ajdari, A., 2004. Engineering flows in small devices: microfluidics toward a lab-on-a-chip. Annu. Rev. Fluid Mech. 36, 381–411.
Fauci, L.J., Gueron, S., 2001. Computational Modeling in Biological Fluid Dynamics, vol. 124. Springer Science & Business Media.
Sheng, J., 2014. Critical review of low-salinity waterflooding. J. Petrol. Sci. Eng. 120, 216–224.
Wörner, M., 2003. A Compact Introduction to the Numerical Modeling of Multiphase Flows. Forschungszentrum Karlsruhe.
Tryggvason, G., Bunner, B., Esmaeeli, A., Juric, D., Al-Rawahi, N., Tauber, W., Han, J., Nas, S., Jan, Y.-J., 2001. A front-tracking method for the computations of multiphase flow. J. Comput. Phys. 169 (2), 708–759.
Sussman, M., Smereka, P., Osher, S., 1994. A level set approach for computing solutions to incompressible two-phase flow. J. Comput. Phys. 114 (1), 146–159.
Hirt, C.W., Nichols, B.D., 1981. Volume of fluid (VOF) method for the dynamics of free boundaries. J. Comput. Phys. 39 (1), 201–225.
Youngs, D.L., 1982. Time-dependent multi-material flow with large fluid distortion. Numer. Meth. Fluid Dynam. 24 (2), 273–285.
Noh, W.F., Woodward, P., 1976. SLIC (simple line interface calculation). In: Proceedings of the Fifth International Conference on Numerical Methods in Fluid Dynamics, June 28–July 2, 1976 Twente University, Enschede. Springer, pp. 330–340.
Baltussen, M., Kuipers, J., Deen, N., 2014. A critical comparison of surface tension models for the volume of fluid method. Chem. Eng. Sci. 109, 65–74.
Brackbill, J., Kothe, D.B., Zemach, C., 1992. A continuum method for modeling surface tension. J. Comput. Phys. 100 (2), 335–354.
Snoeijer, J.H., Andreotti, B., 2013. Moving contact lines: scales, regimes, and dynamical transitions. Ann. Rev. Fluid Mech. 45, 269–292.
Renardy, M., Renardy, Y., Li, J., 2001. Numerical simulation of moving contact line problems using a volume-of-fluid method. J. Comput. Phys. 171 (1), 243–263.
Dussan, E., 1979. On the spreading of liquids on solid surfaces: static and dynamic contact lines. Ann. Rev. Fluid Mech. 11 (1), 371–400.
Sui, Y., Ding, H., Spelt, P.D., 2014. Numerical simulations of flows with moving contact lines. Ann. Rev. Fluid Mech. 46, 97–119.
Mittal, R., Iaccarino, G., 2005. Immersed boundary methods. Annu. Rev. Fluid Mech. 37, 239–261.
Peskin, C.S., 1972. Flow patterns around heart valves: a numerical method. J. Comput. Phys. 10 (2), 252–271.

Deen, N.G., van Sint Annaland, M., Kuipers, J., 2009. Direct numerical simulation of complex multi-fluid flows using a combined front tracking and immersed boundary method. Chem. Eng. Sci. 64 (9), 2186–2201.
Suh, Y., Son, G., 2009. A sharp-interface level-set method for simulation of a piezoelectric inkjet process. Numer. Heat Transfer, Part B: Fund. 55 (4), 295–312.
Sun, X., Sakai, M., 2016. Numerical simulation of two-phase flows in complex geometries by using the volume-of-fluid/immersed-boundary method. Chem. Eng. Sci. 139, 221–240.
Washino, K., Tan, H., Salman, A., Hounslow, M., 2011. Direct numerical simulation of solid-liquid-gas three-phase flow: fluid-solid interaction. Powder Technol. 206 (1), 161–169.
Prosperetti, A., 2002. Navier-Stokes numerical algorithms for free-surface flow computations: An overview. In: Drop-Surface Interactions. Springer, pp. 237–257.
Das, S., Deen, N.G., Kuipers, J.A.M., 2017. Immersed boundary method (IBM) based direct numerical simulation of open-cell solid foams: hydrodynamics. AIChE J. 63 (3), 1152–1173.
Deen, N.G., Kriebitzsch, S.H., van der Hoef, M.A., Kuipers, J., 2012. Direct numerical simulation of flow and heat transfer in dense fluid-particle systems. Chem. Eng. Sci. 81, 329–344.
Van Sint Annaland, M., Deen, N., Kuipers, J., 2005. Numerical simulation of gas bubbles behaviour using a three-dimensional volume of fluid method. Chem. Eng. Sci. 60 (11), 2999–3011.
Bunner, B., Tryggvason, G., 2002. Dynamics of homogeneous bubbly flows Part 1. Rise velocity and microstructure of the bubbles. J. Fluid Mech. 466, 17–52.
Fujita, M., Koike, O., Yamaguchi, Y., 2015. Direct simulation of drying colloidal suspension on substrate using immersed free surface model. J. Comput. Phys. 281, 421–448.
Yokoi, K., 2014. A density-scaled continuum surface force model within a balanced force formulation. J. Comput. Phys. 278, 221–228.
Deen, N.G., van Sint Annaland, M., Kuipers, J., 2004. Multi-scale modeling of dispersed gas-liquid two-phase flow. Chem. Eng. Sci. 59 (8), 1853–1861.
Sussman, M., 2001. An adaptive mesh algorithm for free surface flows in general geometries. Adapt. Meth. Lines, 207–227.
Saha, A.A., Mitra, S.K., 2009. Effect of dynamic contact angle in a volume of fluid (VOF) model for a microfluidic capillary flow. J. Coll. Interf. Sci. 339 (2), 461–480.
Voinov, O., 1976. Hydrodynamics of wetting. Fluid Dynam. 11 (5), 714–721.
Cox, R., 1986. The dynamics of the spreading of liquids on a solid surface. Part 1. Viscous flow. J. Fluid Mech. 168, 169–194.
Lauga, E., Brenner, M., Stone, H., 2007. Microfluidics: the no-slip boundary condition. In: Springer Handbook of Experimental Fluid Mechanics. Springer, pp. 1219–1240.
Lavi, B., Marmur, A., 2004. The exponential power law: partial wetting kinetics and dynamic contact angles. Coll. Surf. A: Physicochem. Eng. Aspects 250 (1), 409–414.
Legendre, D., Maglio, M., 2015. Comparison between numerical models for the simulation of moving contact lines. Comp. Fluids 113, 2–13.
Karagadde, S., Bhattacharya, A., Tomar, G., Dutta, P., 2012. A coupled VOF-IBM-enthalpy approach for modeling motion and growth of equiaxed dendrites in a solidifying melt. J. Comput. Phys. 231 (10), 3987–4000.